JOURNAL OF OPTOELECTRONICS AND ADVANCED MATERIALS Vol. 8, No. 5, October 2006, p. 1775 - 1779

Electron microscopy study of (Fe-Co)-Nb-Si-B alloys

D. M. KEPAPTSOGLOU, G. POLYCHRONIADIS[a], K. G. EFTHIMIADIS[a], P. SVEC[b], E. HRISTOFOROU
Laboratory of Physical Metallurgy, National Technical University of Athens,
9 Heroon Polytechniou str., Zografou Campus, Athens, 15780, Greece
[a]*Physics Department, Aristotle University of Thessaloniki, GR-54124, Thessaloniki, Greece*
[b]*Institute of Physics, Slovak Academy of Sciences, Dubravska cesta 9, 845 11 Bratislava, Slovakia*

Phases produced during crystallization of $(Fe_1Co_4)_{73}Nb_7Si_5B_{15}$ amorphous alloy were studied by means of conventional and *in-situ* heating transmission electron microscopy. Differences in structure, morphology and grain size distributions are discussed. Apparent discrepancies in crystallization kinetics in thinned - originally amorphous, *in-situ* annealed samples versus samples a-priori annealed and thinned are shown to originate from sample dimensions and preparation methods. Information thus obtained is used for indication of the importance of surface and bulk effects during phase transformations. Results are correlated with the classical analysis of transformations from amorphous state.

(Received September 9, 2006; accepted September 13, 2006)

Keywords: Electron microscopy, Nanocrystalline alloys, Crystallization kinetics, Phase transformations

1. Introduction

Transition from amorphous state takes place typically in two-stage transformation process. The first stage represents formation of (nano)crystalline grains from amorphous matrix. The grains are as a rule spherical or regular in shape and their morphology as well as size and spatial distribution is well in agreement with the notion of intense, probably homogeneous, nucleation and three-dimensional growth with low level of mutual impingement among them [1]. Further specific features are related from case to case with the nominal composition and the local ordering in the amorphous state [2,3]. Majority of cases, however, considers the transformation as related to the entire volume of the sample, with surface effects playing important role only in certain instances.

The investigation of the complete process of transition from amorphous through nanocrystalline into a final stable polycrystalline state will be presented on the case of Fe-Co-Nb-Si-B rapidly quenched ribbon, composition close to Co- containing Finement or Si- containing Hitperm [4,5]. The focus will be placed on the morphology of forming phases during crystallization in two types of sample geometry with different thickness, comparing the stability of amorphous state and the kinetics of the transformation in two and three-dimensions.

2. Experimental

Master alloy of $(Fe_1Co_4)_{73}Nb_7Si_5B_{15}$ composition was prepared from elements with purity better than 99.5%. Amorphous ribbons 6mm wide and approximately 25 m thick were prepared by planar flow casting method. Chemical analysis of the ribbons was preformed by inductively coupled plasma spectroscopy. The amorphous state of the ribbons was verified by X-ray and electron diffraction.

Differential thermal analysis measurements were preformed in the Perkin Elmer DTA 7 instrument in nitrogen protective atmosphere with a heating rate of 5K/min. Electrical resistivity was measured by the high precision four probe method, using sharp needle contacts with springs in vacuum using linear heating regime with different heating rates (ranging from 1.25 to 40 K/min) and isothermal annealing. Resistivity including temperature variation was measured with an accuracy of 0.01%. The saturation magnetization (at B=1T) was measured with a vibrating sample magnetometer, during linear heating from room temperature up to 1200K at a rate of 5K/min and subsequent cooling. The samples were ribbon fractions, with a total mass of approximately 20 mg.

Samples for X-ray diffraction analysis were annealed in a vacuum furnace at the pressure better than 10^{-3} Pa and temperature controlled with accuracy better than 0.1K. The X-ray diffraction measurements were performed in Bragg - Brentano geometry using CuK_a radiation with a graphite monochromator in the diffracted beam. Standard 3mm discs for transmission electron microscopy (TEM) were cut from amorphous ribbons. After heat treatment, the discs were thinned by ion beam thinning using the GATAN PIPS. Transmission electron microscopy (TEM) and electron diffraction were performed using JEM 1200EX electron microscope. Transmission electron microscopy observations were also performed during *in-situ* heating with JEOL 100CX TEM equipped with a hot stage. Starting from room temperature, after every 25K the specimen was left to stabilize thermally for half an hour before observation.

3. Phase transformations

Phase transformations during crystallization of the $(Fe_1Co_4)_{73}Nb_7Si_5B_{15}$ were studied by means of classical analysis (Fig. 1). The evolution of normalised electrical resistivity during linear heating and DTA trace are plotted

in the same graph with the evolution of saturation magnetization with temperature for the same heating rate. It can be readily seen that the measurements are in excellent agreement with each other concerning the indication of the phase change in the sample during heating.

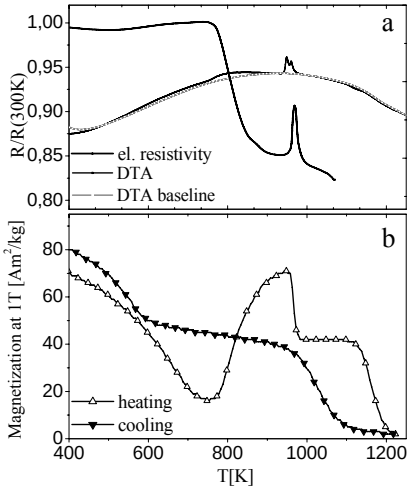

Fig. 1. (a) Evolution of electrical resistivity and DTA trace during linear heating 5K/min and (b) evolution of magnetization during linear heating and cooling 5K/min of as-quenched $(Fe_1Co_4)_{73}Nb_7Si_5B_{15}$ alloy.

Electrical resistivity curve shows a drop starting at around 750K up to almost 950K, followed by a sharp peak round 965K while the DTA trace has a broad exothermic peak between 750K and 950K followed by a double exothermic peak round 960K. The temperature dependence of magnetization after the ferro-to-paramagnetic transition of the amorphous phase round 720K, an increase from 750 up to 950K indicates the formation of a ferromagnetic phase in the amorphous matrix. This is followed by a sharp decrease down to almost half the maximum magnetization value, obtained in the previous stage. The magnetization remains constant up to almost 1150K where a further decrease leads the sample to paramagnetic state. The cooling curve shows a rather large hysteresis with respect to the heating curve with two para-to-ferromagnetic transitions below 1100 and 600K respectively.

The phases formed during the phase transformations were identified in detail by X-ray and electron diffraction. The formation of the ferromagnetic bcc α-FeCo phase is confirmed during the first crystallization stage that takes place in the 750-950K interval (curve b in Fig. 2, Fig. 3 (right)). The crystalline volume fraction of the bcc phase was estimated to be 40 vol.% from the relative area of the {110} peak using Gaussian functions for both the amorphous and nanocrystalline contributions. The average grain size was estimated ~8nm from the broadening of the {110} peak by the Scherrer formula.

Further heating of the sample induces the formation of a fcc-$(FeCo)_{23}B_6$ phase (τ-phase after [6]) rich in B and Nb [7] in the residual amorphous matrix surrounding the α-FeCo grains (curves c, d in Fig. 2, Fig. 3.(left)). This formation takes place in two very fast stages over a very narrow temperature interval of 10K as reflected by the sharp peak of the R(T) curve and the double peak of the DTA trace round 960K. The τ-phase, paramagnetic at these temperatures, is growing initially at the expense of the α-FeCo phase, decreasing thus the magnetization value upon its formation. Further growth of the α-phase, forming from the amorphous remains, is not visible on the magnetization curve due to its paramagnetic state. The former was confirmed by detailed X-ray diffraction analysis around the resistivity peak (curves c, d in Fig. 2), which shows a decrease of the α-FeCo peaks against an increase of the peaks corresponding to the τ-phase. Supersaturation of α-FeCo with both cobalt and metalloid can account for the first-stage formation of the τ-phase due to its diffusion within (nano)crystalline grains towards the grain boundaries, providing favourable conditions for such process.

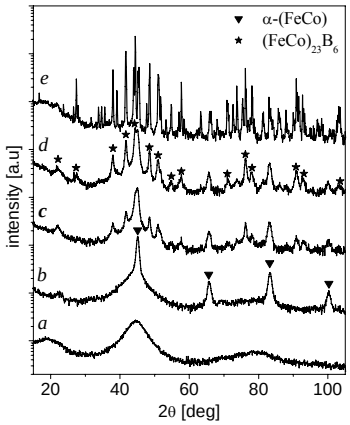

Fig. 2. X-ray diffraction patterns of amorphous as-quenched (a), nanocrystalline (b), formation of $(FeCo)_{23}B_6$ (c) fully crystalline (d) and re-crystallized $(Fe_1Co_4)_{73}Nb_7Si_5B_{15}$ samples (e).

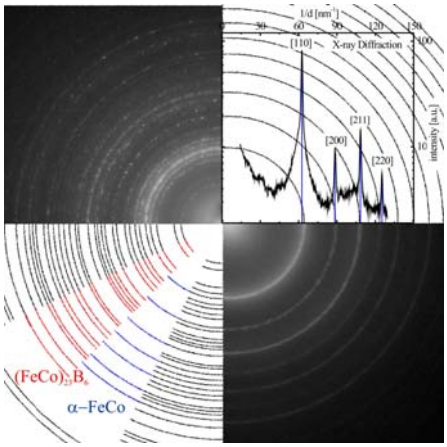

Fig. 3. SAED patterns and simulated diffraction rings of $(Fe_1Co_4)_{73}Nb_7Si_5B_{15}$ samples annealed for 30 min at 923K (right) and 973K (left), respectively.

After annealing at temperatures over 1100K the peaks of the α-FeCo (probably rich in Co due to high nominal content of the element in the sample) vanish from the x-ray diffraction patters. At the same time new peaks corresponding to phase with parameters similar to tetragonal Fe_2B appear. The increase of magnetization below 1100 K probably corresponds to the Curie temperature of the newly formed phase. The last increase of the magnetization upon cooling takes place at the

temperature corresponding to the Curie temperature of the $(FeCo)_{23}B_6$.

Activation energies were calculated from resistivity heating curves, using Kissinger plot (Fig. 4). Peak temperatures were determined by the first derivative of electrical resistivity drop during the formation of α-FeCo and both sides of the resistivity peak during the formation of the τ-phase. Activation energies are relatively high, reflecting the high stability of the amorphous structure: 301kJ/mol for the α-FeCo phase and 662 and 552 kJ/mol for the first and second stage of the $(FeCo)_{23}B_6$ formation, respectively. The lower value for the second stage of $(FeCo)_{23}B_6$ formation suggests that the first stage of the process is responsible for the nucleation and growth of the τ-phase while the second stage transformation is facilitated by the presence of the already formed phase, having a more pronounced growth-like character. This is witnessed by the characteristic shift of the second part of the R(T) anomaly (resistivity decrease) to lower temperatures [8] after heating up to 960K, cooling and repeated heating, as indicated on a cyclic R(T) dependence shown in Fig. 5 (positions 3 and 4, respectively).

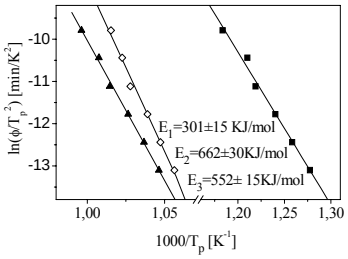

Fig. 4. Estimation of activation energies from linear heating measurements, using the Kissinger plot: E_1 activation energy of formation of α-FeCo and $E_{2,3}$ activation energies of formation of the $(FeCo)_{23}B_6$ phase as determined from the slopes (increase and decrease respectively) of the resistivity peak round 970 K (see also Figs. 1 and 5.).

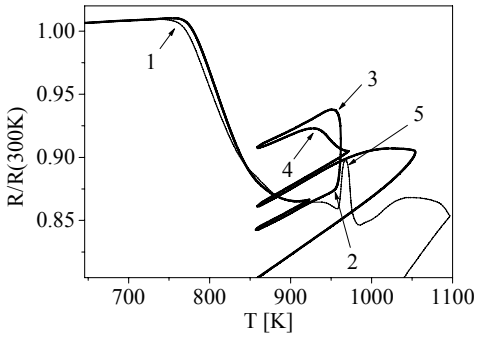

Fig. 5. Cyclic R(T) dependence of as-quenched $(Fe_1Co_4)_{73}Nb_7Si_5B_{15}$ alloy, using linear heating of 5K/min, up to the end of nanocrystallization (930K), close to the maximum of the resistivity peak (960K), end of resistivity peak and 1050K with intermediate cooling run of 5K/min down to 850K. Points on the curve correspond to: (1) nanocrystallization, (2) onset of R(T) peak & formation of the τ-phase, (3) close to peak maximum - cycle turning point, (4) R(T) peak maximum. Linear heating curve R(T) using 5K/min was plotted for comparison. Note the temperature shift between points (4) and (5).

4. Electron microscopy

The final stage of nanocrystallization prior to the process of formation of the τ-phase, with grains of about 10 nm embedded in amorphous matrix is shown in Fig. 6a. The micrograph in Fig 6b corresponding to the state close to the end of the increase of the R(T) anomaly, shows the initial stages of formation of the τ-phase identified by SAED, Fig. 3 left, in form of larger (> 50 nm) objects with lower contrast, around several small α-FeCo grains with decreased contrast. With proceeding transformation the phase evolves into polyhedral grains with well-defined boundaries and the formerly nanocrystalline bcc-grains become less abundant (fig. 8f), in accord with X-ray observations (curve e in fig. 2).

Example of indexing of *SAED* patterns is shown in Fig. 3. Simulated diffraction rings [9] are plotted together with X-ray diffraction pattern of the same sample, for the end of nanocrystallization (Fig. 3 right).

The kinetics, structure and morphology of the produced phases were studied by series of samples prepared conventionally for TEM observations (annealing and subsequent polishing) and samples annealed *in-situ* using the hot stage of the electron microscope. Results can be seen in Figs. 7 and 8 for the *in-situ* and conventional treatment respectively.

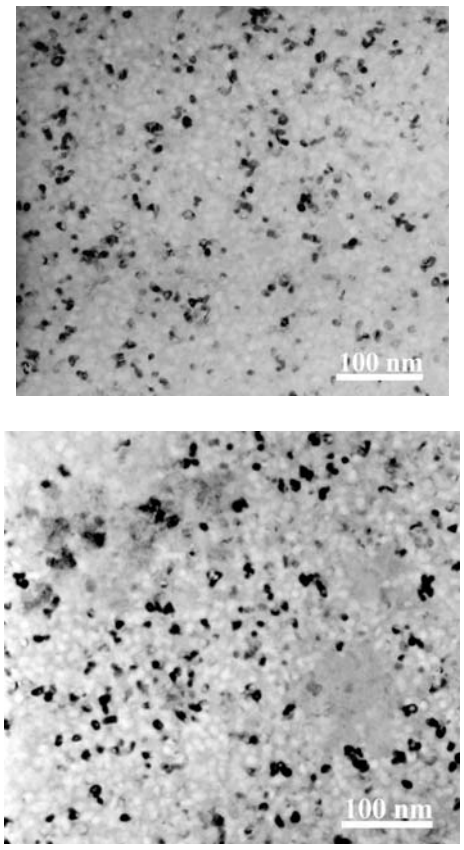

Fig. 6. TEM bright field images of $(Fe_1Co_4)_{73}Nb_7Si_5B_{15}$ samples showing: (a) α-FeCo grains embedded in amorphous remains at the end of the first crystallization stage and (b) onset of $(FeCo)_{23}B_6$ formation (samples annealed at 923K for 30 and 60 min, respectively).

It can be readily seen that although according to the classic kinetic analysis nanocrystallization does not start until 750 K, signs of crystallinity in the sample annealed *in-situ* are visible at temperatures as low as 628 K (Fig. 7a), while the $(FeCo)_{23}B_6$ phase can be detected at temperatures around 823 K (Fig. 7b). For conventionally annealed samples, as expected, no sign of crystallinity appears until 750 K. Different stages of growth of the α-FeCo phase embedded in amorphous remains can bee seen in Fig. 8a, b, for samples annealed for 30 min at 823 K and 923 K, respectively, and Fig. 6a for a sample annealed for 30 min at 973 K where the maximum crystallinity content is reached.

The apparent temperature and crystallization kinetic discrepancies between the two sets of samples originate from the different principles of the two methods used. While in the case of conventionally treated samples crystallization is controlled by volume-induced nucleation and three-dimensional growth, crystallization of samples annealed in situ reflects "thin film" behavior. The sample thicknesses are very small in order to allow observation in the microscope. In such cases nucleation is surface induced and enhanced due to the increased number of sites available for heterogeneous nucleation; two-dimensional growth can be expected to be favored due to small sample thickness, resulting in effectively decreased phase stability and accelerated kinetic phenomena [10].

The main result of different growth dimensionality is the morphology of the produced phases. While in the case of conventionally annealed samples α-FeCo spherulitic grains are dispersed in the amorphous remains, their shape in the case of the *in-situ* annealed sample differs significantly and assumes a more irregular "drop-on-surface" character given by anisotropic growth rate in different directions.Grain size distributions measured by software especially designed for this purpose [11] for small grains (Figs. 7, 8) show increased grain sizes of more than 25 nm for the *in-situ* annealed samples after nanocrystallization as compared with ~ 10 nm for conventionally annealed samples. Furthermore, there is a progressive increase of the size of nanograins in the former case (Fig. 7b) while the size of the α-FeCo grains in Fig. 8b does not evolve significantly with proceeding transformation; the presence of the τ-phase may account for the grain sizes of ~ 30 nm in Fig. 7b at the given stage of transformation. The final crystallization stage (above 960K) leads to large grains of the τ-phase; however, *in-situ* transformation yields significantly larger grain sizes ranging from ~ 50 to ~ 100 nm while conventional procedure leads to grain sizes rarely exceeding 50 nm (Figs. 7c and 8c). The gap in both distributions is related with the presence of two types of grains, the smaller corresponding to the α-FeCo phase. Again, thin-film like character of transformation is reflected in increased dimensions of transformation products as well as in unstable sizes of the nanograins.

Surface phenomena are in general not taken into account when studying crystallization kinetics of ribbon samples by considering them *a-priori* infinite media. Accurate interpretation of transformation phenomena, however, should take the sample dimensions and surface phenomena into account, especially in cases where size and morphology of newly formed phases are sensitive to mechanisms controlling the transformation kinetics.

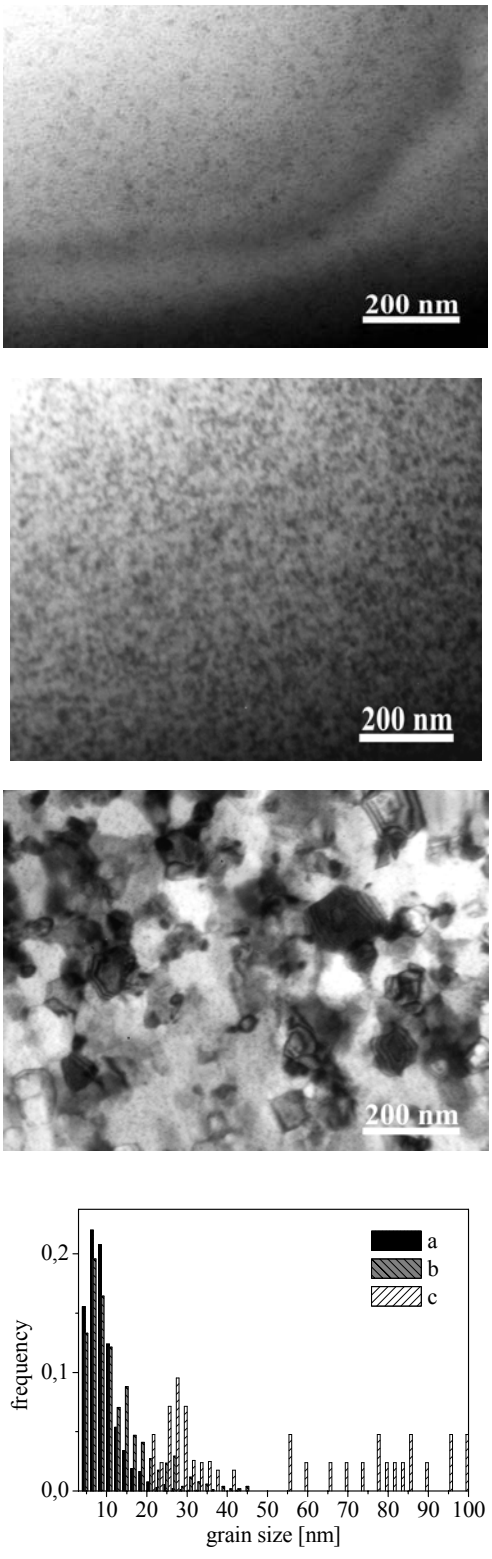

Fig. 7. TEM bright field images of $(Fe_1Co_4)_{73}Nb_7Si_5B_{15}$ samples annealed in-situ at (a) 628, (b) 823 and (c) 1013 K and the corresponding grain size distributions.

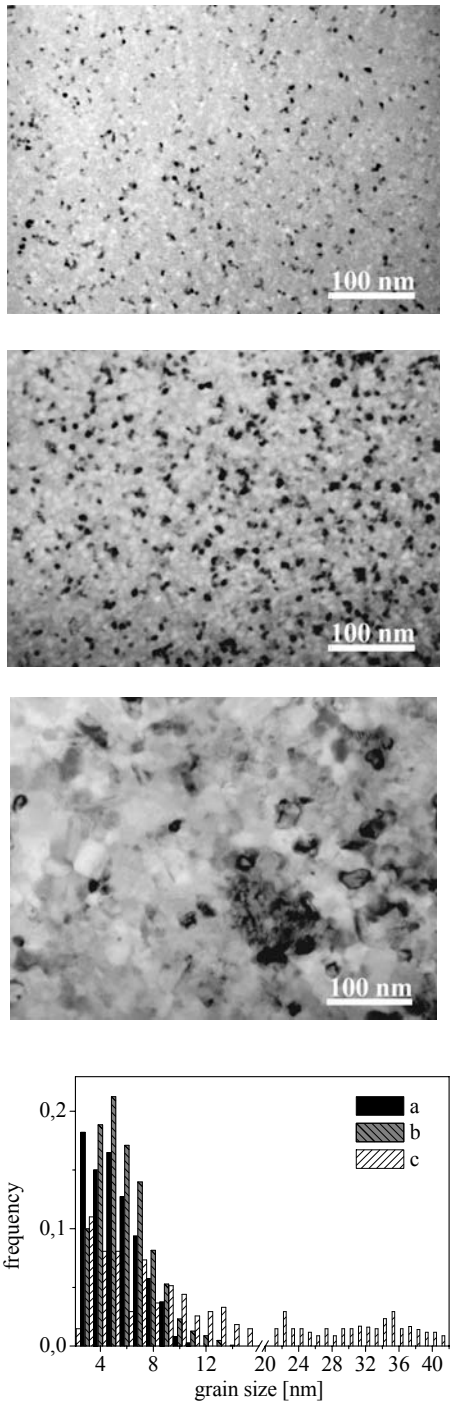

Fig. 8. TEM bright field images of $(Fe_1Co_4)_{73}Nb_7Si_5B_{15}$ samples annealed conventionally for 30min at (a) 803, (b) 873 and (c) 923 K and the corresponding size distributions.

Acknowledgements

The authors would like to acknowledge support from the PENED 2001 01ED93 of the Hellenic General Secretariat of Research and Technology, the Slovak GAS (VEGA 5/5096/25, APVT-51-052702, APVT-51-021102 and SO 51/03R8 06 03) and Centre of Excellence of SAS 'Nanosmart'.

References

[1] R. Hasegawa, J. Optoelectron. Adv. Mater. **6**, 503 (2004).
[2] P. Svec, K. Kristiakova, J. Optoelectron. Adv. Mater. **4**, 223 (2002)
[3] K. Kristiakova, P. Švec, D. Janickovic, Mater. Trans. JIM, **42**, 1523 (2001)
[4] M. A. Willard, D. E. Laughlin, M. E. McHenry, J. App. Phys., **87,** 7091 (2000)
[5] C. Miguel, A.P. Zhukov, J.J. del Val , A. Ramirez de Arellano and J. González, J. App. Phys. **97,** 034911 (2005)
[6] Y. Khan and H. Wibbeke, Z. Metallk. **82**, 705 (1991).
[7] D. M. Kepaptsoglou, M. Deanko, D. Janickovic, E. Hristoforou, I. Skorvanek and P. Svec, Mater. Sci. Eng. A (2005), *submitted*
[8] E. Illekova, Thermochim. Acta, **387,** 47 (2002).
[9] J. L. Labar**,** Microscopy and Analysis, **75**, 9 (2002).
[10] V. I. Trofimov, I.V. Trofimov, J.I. Kim, Nucl. Instrum. Meth. B, **16**, 334 (2005).
[11] M. Deanko, D.M. Kepaptsoglou, D. Muller, D. Janickovic, I. Skorvanek, E. Hristoforou, P. Svec, J. Electron Microsc. (2005), *in print*.

*Corresponding author: eh@metal.ntua.gr